https://doi.org/10.1038/s44310-024-00014-9

Resonator embedded photonic crystal surface emitting lasers

Zijun Bian[1] ✉, Xingyu Zhao[1], Jingzhao Liu[1], Daehyun Kim[1,2], Adam F. McKenzie[1], Stephen Thoms[1], Paul Reynolds[1], Neil D. Gerrard[1], Aye S. M. Kyaw[1], James Grant[1], Katherine Rae[1], Jonathan R. Orchard[3], Calum H. Hill[3], Connor W. Munro[1,3], Pavlo Ivanov[3], David T. D. Childs[3], Richard J. E. Taylor[3] & Richard A. Hogg[1,2]

The finite size of 2D photonic crystals results in them being a lossy resonator, with the normally emitting modes of conventional photonic crystal surface emitting lasers (PCSELs) differing in photon lifetime via their different radiative rates, and the different in-plane losses of higher order spatial modes. As a consequence, the fundamental spatial mode (lowest in-plane loss) with lowest out-of-plane scattering is the primary lasing mode. For electrically driven PCSELs, as current is increased, incomplete gain clamping results in additional spatial (and spectral) modes leading to a reduction in beam quality. A number of approaches have been discussed to enhance the area (power) scalability of epitaxy regrown PCSELs through careful design of the photonic crystal atom[1–3]. None of these approaches tackle the inflexibility in being unable to independently modify the photon lifetime of the different modes at the Γ_2 point. As a method to introduce design flexibility, resonator embedded photonic crystal surface emitting lasers (REPCSELs) are introduced. This device, combining comparatively low coupling strength photonic crystal structures along with perimeter mirrors, allow a Fabry–Pérot resonance effect to be realised that provides wavelength selective modification of the photon lifetime. We show that surface emission of different surface emitting modes may be selectively enhanced, effectively changing the character of the modes at the Γ_2 point. This is a consequence of the selective modification of in-plane loss for particular modes, and is dependent upon the alignment of the photonic crystal (PhC) band-structure and distributed Bragg reflectors' (DBRs) reflectance spectrum. These findings offer new avenues in surface emitting laser diode engineering. The use of DBRs to reduce the lateral size of a PCSEL opens the route to small, low threshold current (I_{th}), high output efficiency epitaxy regrown PCSELs for high-speed communication and power sensitive sensing applications.

Photonic crystal surface emitting lasers (PCSELs) have recently emerged as a new class of laser diode that utilize 1st and 2nd order Bragg diffraction to realise surface emitting lasers with large area[4]. By engineering the PCSEL design, several functionalities have been reported, including on-chip beam steering[5–7], varying the beam pattern[8], polarization control[9], ultrafast photonics[10,11], area (power)-scalability, and high beam quality lasing[1,2,12–15]. PCSELs have been reported spanning the ultraviolet[16], near-infrared[15,17–19], mid infrared[20], and the terahertz spectral regions[21].

PCSELs are of significant recent interest due to their suitability for a range of applications, including light detection and ranging (LiDAR)[22] and free space communications[23,24]. Initially, PCSELs were achieved through wafer fusion[25], but epitaxial regrowth[26] is now widely used, avoiding undesirable defect states at the fusion interface[27], enabling high power operation. According to the regrowth conditions, either voids or all-semiconductor structures can be selected[18,26]. High-power PCSELs with voids have been previously realized through metalorganic vapour-phase

[1]James Watt School of Engineering, University of Glasgow, Glasgow G12 8QQ, UK. [2]Aston Institute of Photonic Technologies, Aston University, Birmingham B4 7ET, UK. [3]Vector Photonics Ltd., Building 4.05, West of Scotland Science Park, Kelvin Campus, 2317 Maryhill Road, Glasgow G20 0SP, UK.
✉e-mail: z.bian.1@research.gla.ac.uk

epitaxy (MOVPE)[1,13–16,28], with investigations into the epitaxial regrowth and void formation processes being recently reported[29].

Figure 1a, b show a schematic of a photonic crystal with a square lattice and circular atoms. The base light waves (green arrows) in such a PhC layer can be diffracted and coupled in either the 1D (±180°) and 2D (±90°) directions (purple arrows) due to the 2nd and 1st order Bragg conditions, represented as (κ_{1D}) and (κ_{2D}) separately. Additionally, the coupled in-plane light waves can also be diffracted into the vertical direction (grey arrow) due to the 1st order Bragg condition, which is the origin of the surface emission. By contrast, the losses of a traditional edge emitting laser are described by the mirror loss (α_m) and internal loss (α_i).

For a PCSEL the mirror loss is equivalent to the external vertical loss ($\alpha_\perp$) providing surface emission due to the 1st order Bragg condition. In addition to α_i, the PCSEL has an additional parasitic loss due to in-plane optical loss ($\alpha_{//}$) as shown in Fig. 1c. These parameters are critical when designing the PhC layer within a device as they determine the device's threshold gain and slope efficiency, which can be expressed as[28]:

$$g_{th} = \alpha_\perp + \alpha_{//} + \alpha_i \quad (1)$$

$$\frac{dP}{dI} = \frac{h\upsilon}{e}\eta_i \frac{\alpha_\perp}{\alpha_\perp + \alpha_{//} + \alpha_i}\eta_{up} \quad (2)$$

where h is the Planck's constant, υ is the mode frequency, the unit charge is e, η_i is the internal efficiency and η_{up} is the upward-radiation loss (output) efficiency. The values of $\alpha_{//}$ & $\alpha_\perp$ are mainly determined by the refractive contrast and shape of the PhC atoms and the device size[14,28,30]. The value of internal loss α_i is decided mainly by the device waveguide structure and free-carrier loss characteristics of the constituent materials.

Figure 1d shows an example of photonic band structure around the Γ_2 point with a square-lattice structure and a circular atom with radius of 0.4a, calculated by the 2D plane-wave expansion (2D-PWE) method[31]. Lasing occurs at the band edges, where the gradient is zero resulting in zero group velocity modes. Therefore, wavelengths at the band edges form standing waves with a high photon density. The selection of the lasing mode (and its stability) is governed by the difference in threshold gain of the different modes. For the modes at the Γ_2 point, threshold gain is determined by the symmetry of the in-plane electric field distributions of each mode, as compared to the node of the electric field distribution[32]. This leads to "leaky" and "non-leaky" modes with comparatively high and low $\alpha_\perp$, respectively. This is presented schematically in Fig. 1d. As the mode separation is much smaller than the gain spectrum of the laser diode active element, the lowest threshold gain mode is selected as the primary lasing mode. If the in-plane optical loss and internal loss are equal for all mode center lasing modes (as has been the case to date), then the lasing mode with the lowest slope efficiency is selected. The details of PCSEL band-structure, and the origins of the lasing mode are discussed in Supplementary Fig. S1. Considering the utilized PhC design parameters in work, the lasing mode is mode D.

There are fundamental issues for PCSEL design: the lasing mode is the mode with the lowest out-of-plane scattering[28], and for simple, symmetric structures, this out of plane scattering may be vanishingly small[33]. Additionally, there is a parasitic loss of lasing power in-plane. For conventional, PCSEL designs with transverse electric (TE) gain and square PhC symmetry, the strength of coupling[34], κL, (where κ is the coupling coefficient, and L is lateral device size), is high as compared to edge emitting DFBs (κL = 2) with κL of ~ 40 (single lattice)[14], ~27 (right angle isosceles triangle)[28], ~25(double lattice)[14]. This high value of κL is required to inhibit the loss of optical power in-plane. In order to obtain high single-mode powers, novel PhC designs have been introduced that increase gain margin between the fundamental and higher order modes, but act to *reduce* the coupling coefficient κ_{1D}, resulting in the need for larger devices[2,14].

Previous studies in PCSELs[28,32] have also shown that modifying the three-dimensional (3D) atom shape, breaking the symmetry of the electric-field distribution can significantly increase $\alpha_\perp$ of the lasing mode, increasing the slope efficiency. However, the performance (threshold gain, slope efficiency) of PCSELs with low vertical radiation loss and high in-plane optical loss caused by a finite size PhC region is mostly determined by $\alpha_{//}$.

Lateral optical confinement has been studied in a range of systems using band-edge resonances of 2D PhC slabs. Finite 2D PhC structures have

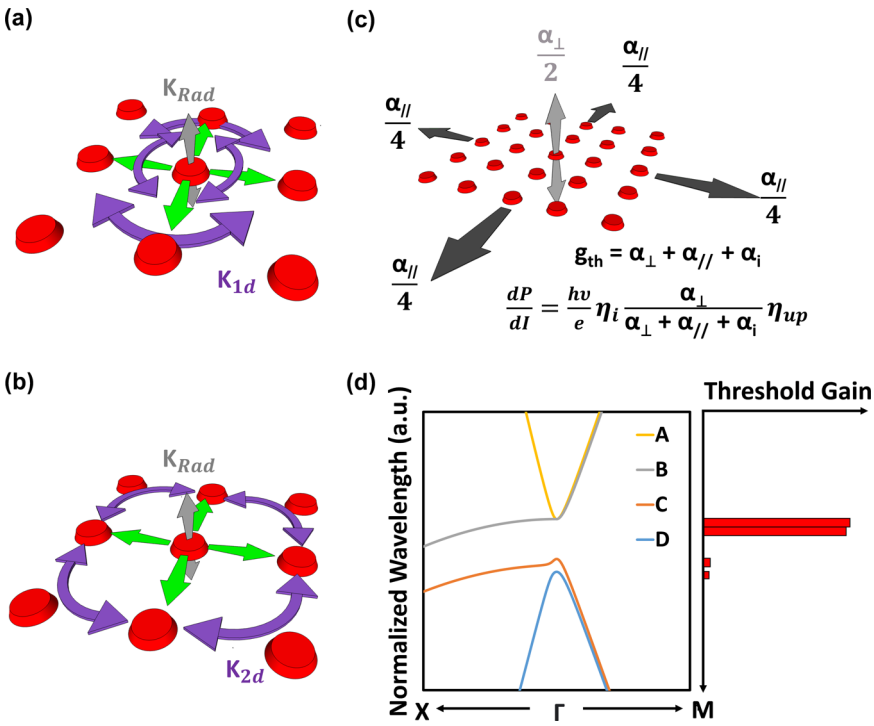

Fig. 1 | Photonic crystal scattering mechanism, and device losses. a A schematic showing the κ_{1D} coupling mechanism between forward and backward directions. **b** A schematic showing the κ_{2D} coupling mechanism between orthogonal in-plane directions. **c** The radiation loss inside a finite size PCSEL. Green arrows represent the base light waves. Purple arrows show the coupling mechanism between two diffracted light waves. Grey arrows are the vertical radiation loss. Black arrows represent the in-plane optical loss. **d** A schematic of a square lattice band-structure and its corresponding threshold gain.

been demonstrated to be lossy resonators, with loss increasing as lateral size is reduced with a finite 2D-PhC with boundary mirrors having properties like an infinite PhC[35]. These effects have been demonstrated using a PhC heterostructure[36–38] or DBR pairs[35,39,40], in a range of optically pumped laser structures, and via cold cavity band-structure analysis. The reduction of in-plane optical loss due to the boundary mirrors has been reported.

For electrically driven PCSELs, the effect of a mirror at the boundary of one side of a square atom symmetry device has recently been discussed via simulation[41]. This study, on a conventional PCSEL with $\kappa_{1D} \sim 1000\ cm^{-1}$ showed that this feedback (varying both phase and reflectivity) influenced the mode frequencies, threshold gain, gain margin, and field intensity of the PCSEL. The effect of cleaved facets (distributed phase difference, reflectivity = 0.32) on one or two sides of a conventional PCSEL with $\kappa_{1D} = \sim 1300\ cm^{-1}$ was explored experimentally[42]. It was demonstrated that this feedback resulted in an alteration of the near-field, reduction in threshold, and increase in slope efficiency. A PhC device utilising photonic band-gap mirrors encapsulating a PCSEL ($\kappa_{1D} = \sim 2500\ cm^{-1}$) has also been simulated[11], predicting a reduction in threshold gain, and indicating that such PCSELs can be shrunk to ~10 μm diameter, resulting in a possible increase in the modulation rate of the PCSEL. In summary, all these PCSEL structures consider the use of mirrors at the boundary of the PCSEL influencing all the modes at the Γ_2 point in the same way, which does not achieve wavelength selectivity, utilizing one mirror[41] (simulation), two mirrors at right angles[42] (experimental), and 2D photonic crystal heterostructure[11] (simulation).

This report introduces a resonator embedded photonic crystal surface emitting laser (REPCSEL). It is constituted of a PhC region surrounded by a 1st order DBR mirror where κL of the PhC is reduced to allow a *resonance* to be formed, as there is a defined path length between the mirrors. This resonance effect allows a wavelength selective modification of the photon lifetime within the PhC region, resulting in a wavelength selective increase in the out-of-plane scattering, due to a wavelength selective modification of the in-plane loss of the different modes. This allows preferential selection/enhancement of the lasing mode, opening up new avenues in surface emitting laser design.

Results and Discussion

The propagating light inside a PhC can be coupled in different ways that depend on the shape of the lattice structure[43]. The square lattice is often chosen for PCSELs because of its comparatively simple band structure at the Γ_2 point where only four modes exist[44] (c.f. triangular lattice[4]). Conventionally, for a PhC with high refractive index contrast and/or large area, a sufficient proportion of the light can be confined inside the PhC region due to a high κL, as shown schematically the modelling result in Fig. 2a (here κL = ~40), but slope efficiency remains low, as compared to other classes of laser diode. Figure 2b shows a schematic of our REPCSEL concept where the PhC region is surrounded by a mirror. All conventional PCSELs will leak a fraction of the in-plane light from the PhC region. This fraction is inversely proportional to κL. For small κL this may result in an impractically high threshold gain. Adding external feedback at the perimeter of such a PhC structure should make it possible to significantly reduce $\alpha_{//}$ and improve device performance. A DBR (1st order 1D PhC) structure on each side of the 2D PhC can function as this mirror to reflect light back into the PhC region with defined phase, as shown schematically. The photon lifetime within the device is therefore increased as $\alpha_{//}$ is reduced. As expected from Eqs. (1) & (2), a reduction in threshold current and the improvement in slope efficiency are expected by a reduction in $\alpha_{//}$.

Significantly, if the κL of the PhC structure is sufficiently low (less than κL = ~10), there remains a well-defined cavity length between the mirrors resulting in a resonance effect [Supplementary Figs. S2, S3]. In Fig. 2c, the calculated reflectivity of one DBR is plotted (dotted black). For a well-defined cavity length (200 μm in this case) a Fabry-Pérot resonator effect may be obtained (solid blue). Here, the combined reflectance of the REPCSEL boundaries varies with wavelength, providing a wavelength dependent variation in photon-lifetime. Also plotted (solid red), is the internal resonance enhancement factor (IREF)[45] which describes the amplified ratio between the enhanced light due to the REPCSEL structure and the transmitted (or leaked) light from the PhC region. This *resonator effect, which is* formed using unsaturated DBR reflectivity *(R < 1 to induce troughs and peaks of resonator reflectivity)* at the PhC perimeter (as in the case of conventional high κL designs), is at the heart of the operation of our device in terms of varying the in-plane-loss, and surface emission of different modes as a function of wavelength. Device design therefore relies upon the alignment of the reflectance and IREF peaks to the PhC band edges.

Figure 3a compares representative current (I)-power(L)-voltage(V) results of 1.3 μm PCSEL and REPCSEL devices. Both devices are from the same wafer and have therefore undergone identical fabrication processes, with the only difference being the additional DBR regions in the REPCSEL. For PCSEL structures, no devices were found to lase up to 1.2 A (~3.2 kA/cm^{-2}). The typical REPCSEL shown, has a threshold current of 324 mA (860 A/cm^2). Current-voltage responses (2-wire measurement, so includes system resistance) of the PCSEL and REPCSEL devices were essentially identical. A slope efficiency of 0.04 W/A, and a power conversion efficiency (PCE) of 2% at 1 A were observed. Whilst these are not the largest values reported for PCSELs, we note that these values are obtained without any vertical reflectors such as a DBR[46], and incorporating a notoriously low output efficiency PC atom shape (circle)[18]. This value therefore compares favourably with the highest reported PCE for 1.3 μm PCSELs of 7% using a double-crystal void PC on the n-side of the junction[15].

The observation of lasing for DBR containing structures is clear evidence of reduced $\alpha_{//}$. Figure 3b plots the spectrum of this REPCSEL device at 550 mA. The linewidth of the REPCSEL is 0.25 nm. A > 42 dB SMSR is observed. The inset shows the nearfield image taken at $I = 1.6*I_{th}$. A far-field divergence of ~3^0 was measured. In the following we focus on wavelength selective modifications to the operation of a REPCSEL, as compared to a PCSEL.

Figure 4a shows the band structure measurement for the same RECPSEL device. The band-structure measurements were taken at $I = 0.4*I_{th}$ to ensure that the cavity is "cold" and that contribution from amplified spontaneous emission to the emission was minimised. The black dotted lines indicate the PhC band structure from simulation. Considering the PhC alone, it is expected that band edges A&B are leaky modes, and C&D are non-leaky modes (see Fig. S1). This should result in stronger surface emission from modes A&B, and considerably weaker surface emission from modes C&D, with the mode with lowest radiative scattering being the lasing mode. Figure 4b plots the emission spectrum at the Γ_2 point. It is clear that both modes have similar surface emission intensity at this low current. Almost identical peak intensities and linewidths (while its resolution is limited by the measurement system) are observed. It is therefore shown that scattering from modes C&D have been selectively enhanced as compared to that from modes A&B. Figure 4c shows the REPCSEL band structure above threshold ($I = 1.2*I_{th}$), indicating the lasing mode. If out-of-plane scattering were equal for all the modes at the Γ_2 point, in the absence of a change in other loss parameters, then we would expect a competition between the bands, and multi-mode lasing to occur. However, the alignment of the DBR reflectance to the PhC band-edges allows mode selectivity due to a significant difference in in-plane loss for modes A&B, and C&D. As we do not wish to have the same enhancement to both leaky and non-leaky modes, DBR number is selected in order to achieve wavelength selective loss is introduced in Fig. 5c, where 100 DBR periods is chosen to maximise in-plane optical loss difference between the leaky and non-leaky modes.

The analysis of the development of the band-structure with applied current allows further insight into the different loss parameters of the possible lasing modes. This data is discussed in Supplementary Fig. S4. Figure 4d plots the intensity of the surface emission at the Γ_2 Point as a function of applied current. At around $I = 0.75*I_{th}$, a clear change in the intensity of the different band-structure features occurs, indicating that a particular spectral region is undergoing regenerative amplification, and is super-luminescent. This prelude to lasing occurs for the C&D band only,

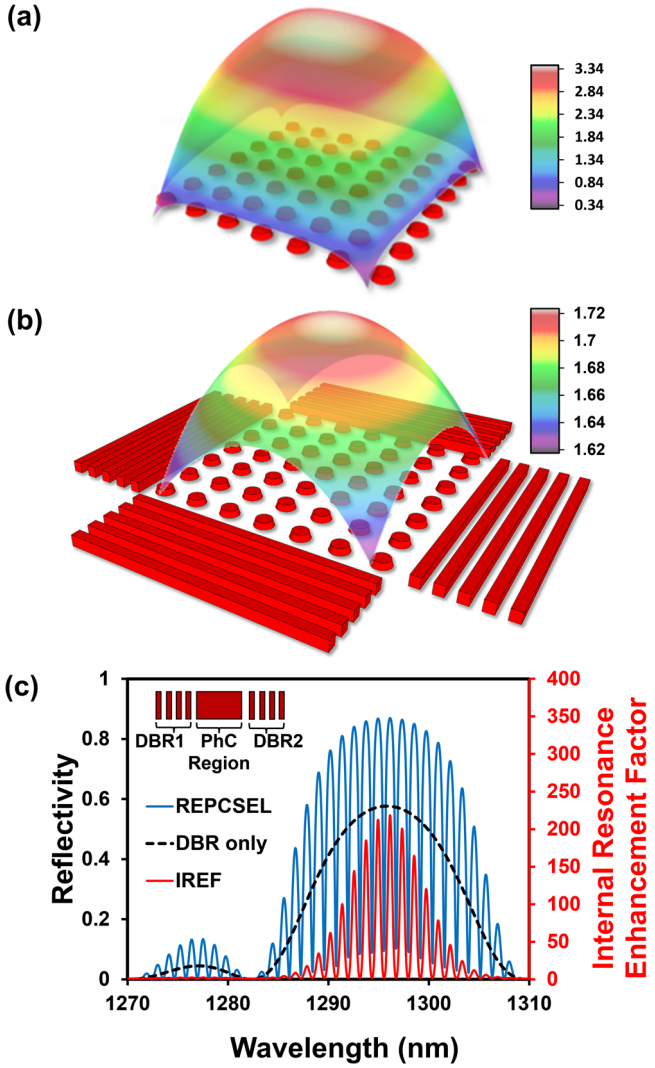

Fig. 2 | Near-field patterns and resonator reflectivity. a Schematic of the simulated near-field for a square lattice PhC layer with κL = ~40. **b** Schematic of the near-field of a REPCSEL structure with κL = ~2. **c** Reflectance simulation of a single DBR structure (in black) which represents either DBR1 or DBR2; REPCSEL structure (in blue) contains DBR1+PhC+DBR2, and associated with internal resonance enhancement factor (in red). Details of the reflectance modelling structure are introduced in the method section.

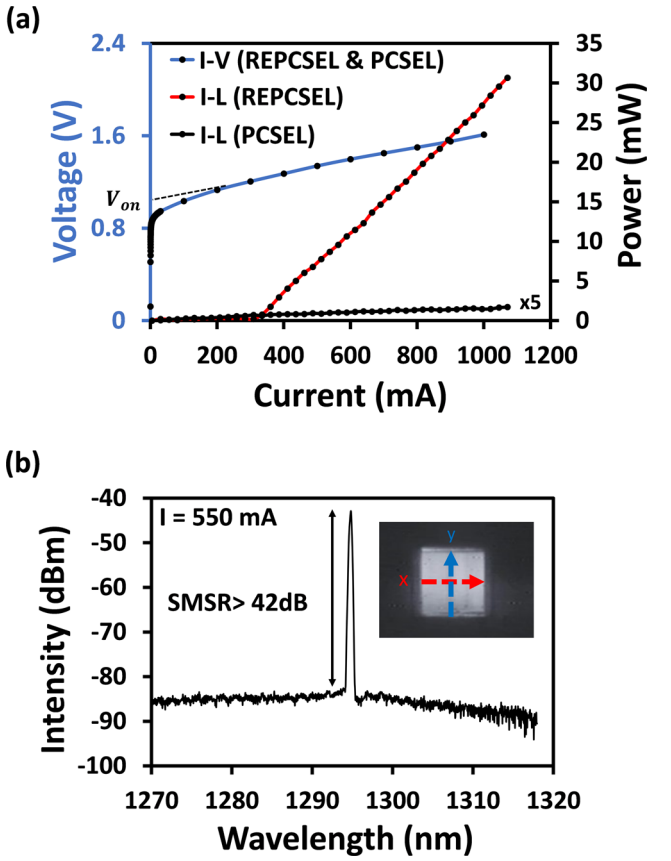

Fig. 3 | Device operating characteristics. a The current-power (I-L) characteristics of PCSEL (dark line) and REPCSEL (red line) devices, measured under pulsed conditions (2% duty cycle,5 μs pulse width). The PCSEL's output power was plotted x5 for ease of comparison. The blue line represents the typical current-voltage (I–V) characteristics of both PCSEL and REPCSEL devices, measured under continuous wave (CW) conditions. A turn-on voltage (V_{on}) of 1.01 V was obtained. **b** The corresponding spectra of REPCSEL with a driven current of 550mA and a spectral resolution of 0.1 nm. A side-mode suppression ratio (SMSR) > 42 dB is observed. The inset shows the near-field image measured at 1A.

indicating that the total optical loss is lower. This is in agreement with the prediction of a reduced in-plane loss, yet equivalent radiative coupling and internal loss.

To understand the mode selection of RECPSEL structure, Fig. 5a plots the calculated reflectance of the Fabry–Pérot resonator and the simulated band-structure for a 200 μm x 200 μm REPCSEL that mentioned in both Figs. 3 and 4, constituted of a PhC with 500 × 500 periods under the p-contact, while a 100 number of DBR is outside the PhC region and the contact. Here, the choice of these dimensions (PhC and DBR number, discussed later), following determination of the PhC band-structure results in the modes at the Γ_2 point; A&B at around 1297 nm, and C&D at around 1295 nm, corresponding to troughs and peaks in the resonator reflectance, respectively. This is the origin of the spectral variation of the in-plane loss, photon lifetime, and IREF of the modes at the Γ_2 point. Figure 5b plots the corresponding variation in IREF for the same device as a function of wavelength in the region of the Γ_2 point. This plot highlights the ability to tune the difference in IREF for the leaky modes(A&B) and non-leaky modes(C&D) by ~200. In the case shown, a trough for one peak is aligned with bands A&B, and a peak (IREF ~ 200) is aligned with bands C&D. It is also noticed both mode C&D are expected to be enhanced equally because of the small (<0.15 nm) splitting between the modes.

Therefore, we attribute lasing at C&D to the nature of the mode that has lowest output plane scattering (mode D). Figure 5(c) plots the calculated in-plane loss (See Supplementary Fig. S2, S3) as a function of the number of DBR pairs for the 200 μm x 200 μm REPCSEL we have described here. As the reflectance spectrum (Fig. 5a) changes with increasing DBR number, the difference in reflectance of peaks and troughs reduces, resulting in the in-plane loss being identical (52 cm^{-1}) for zero DBRs, and converging (~a few cm^{-1}) for large DBR number. For intermediate DBR number, a significant difference in in-plane loss is obtained for the leaky and non-leaky modes. For the devices presented here, in order to achieve a large loss difference, 100 DBR pairs are implemented, which gives a ~79% difference in resonator reflectance.

For the work reported here, a square symmetry PhC and square PCSEL are utilised with κL~2. For a PhC with triangular symmetry, a similar design should be possible. However, for a PCSEL with more complex device shape (oblong, triangle) the REPCSEL will work in a different manner, and will be the topic of future work.

In order to further confirm the attribution of wavelength selection to the alignment of modes at Γ_2 point to the multi IREF peaks, Figures S5 and S6 show the comparison between PCSEL, and REPCSEL structures with different DBR structures targeting different wavelengths (1550 nm, 1542 nm, 1534 nm) to tune the envelope of resonance peaks through the

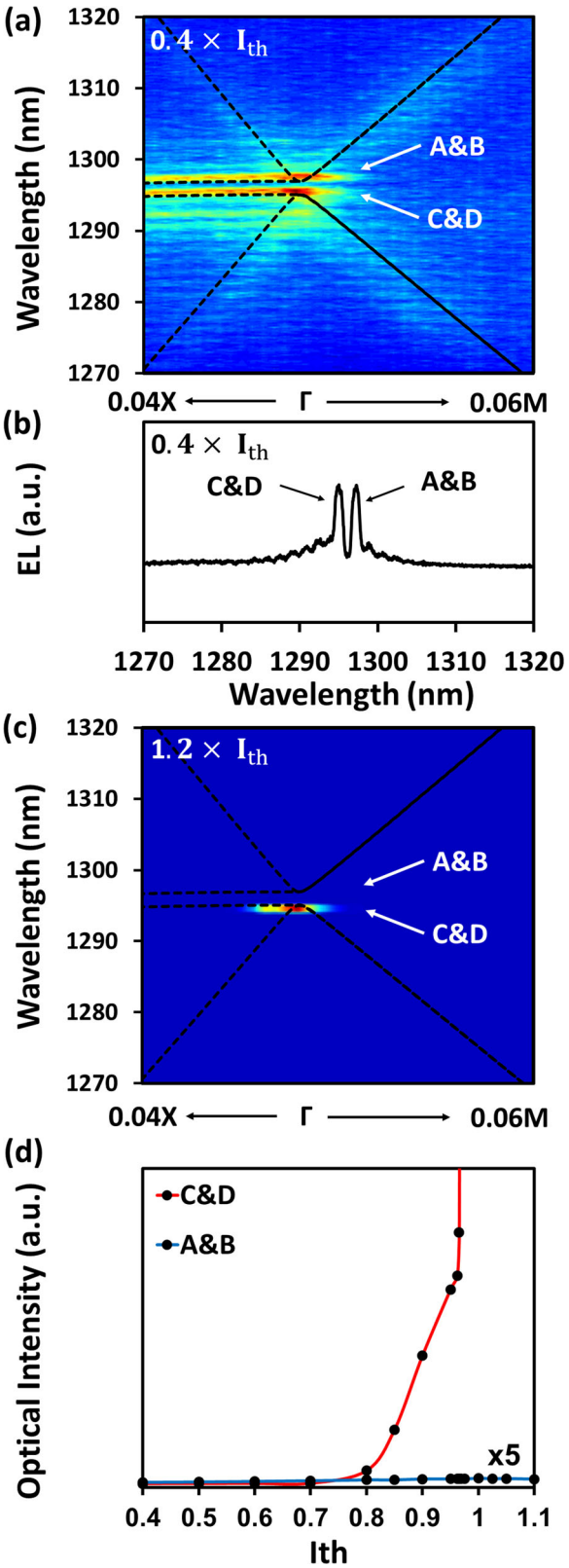

Fig. 4 | Band-structure analysis. a The measured band structure of the REPCSEL at I = 0.4 × I_{th}. The black dotted lines show the simulated band structure. **b** The corresponding electroluminescence(EL) spectra at the Γ_2-point. **c** The measured band structure at I = 1.2 × I_{th}. The degenerate band edges (A & B) and nondegenerate band edges (C & D) are highlighted. **d** The maximum optical intensity of the band edges as a function of drive current. The optical intensity of modes (A&B) was plotted x5 for ease of comparison.

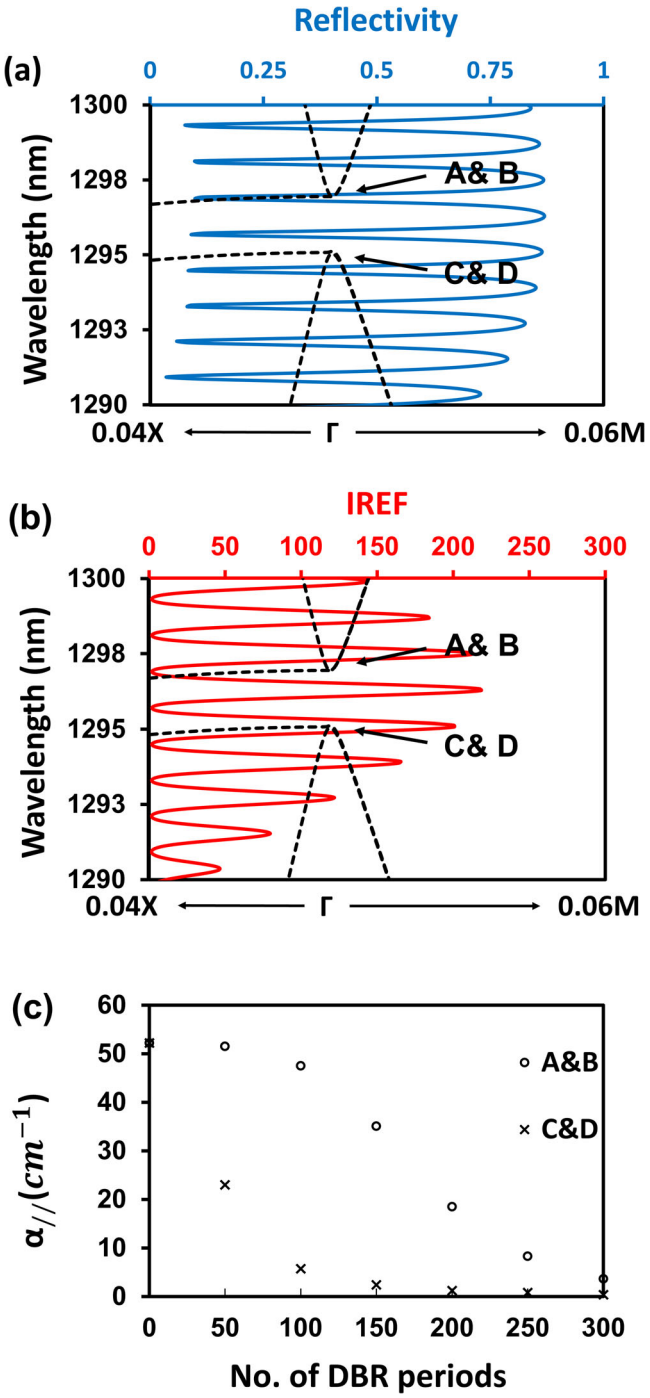

Fig. 5 | Resonator reflectivity, band-structure, and in-plane loss simulation. a The simulated reflectance of the REPCSEL with a DBR targeted wavelength at 1297 nm. **b** Its calculated IREF value. **c** The simulated in-plane optical loss of a 1.3 μm REPCSEL for the two band-edges as a function of perimeter DBR pairs. The maximum in-plane optical loss difference between leaky and non-leaky modes can be found at 100 number of DBR periods.

PhC band-structure. By measuring their band structures below I_{th}, the movement of IREF peaks and the selection of leaky or non-leaky modes to be enhanced can be clearly seen. It can be deduced that by tunning the DBR target wavelength, it is possible to force any modes at the Γ_2 point to be the primary lasing mode. As lateral confinement is based on the alignment of the expected lasing mode with the IREF peak, how this type of alignment can be affected by carrier and thermal effects is under investigation.

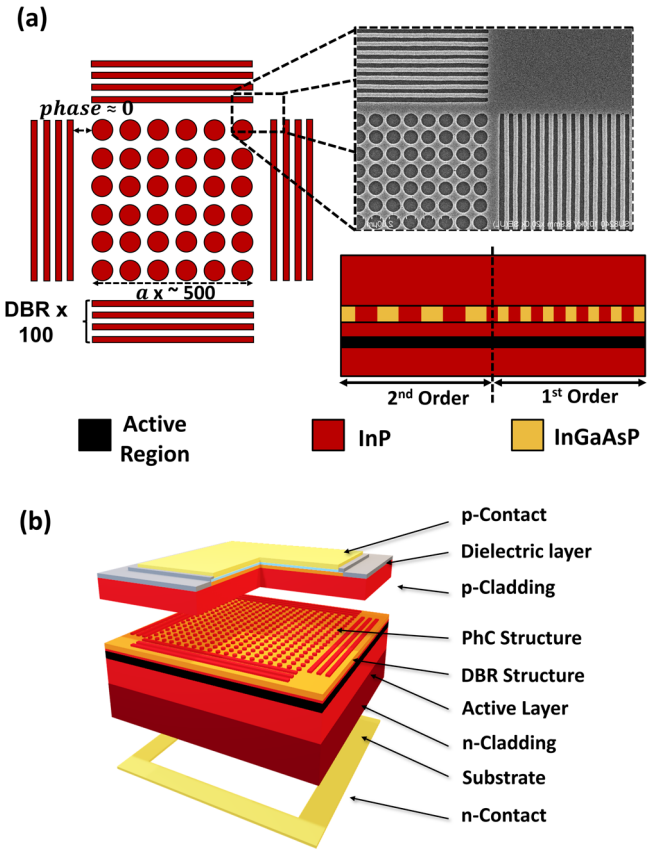

Fig. 6 | Device fabrication and structure. a The schematic of a 1.3 μm REPCSEL with SEM micrograph (after e-beam lithography), and a plan-view schematic of the device cross section. **b** The 3-D schematic of the device structure.

In conclusion, we have described the concept for the REPCSEL, with epitaxy regrown device examples at 1.3 μm and 1.5 μm (in Supplementary), where low κL PhC structures are bound by a DBR perimeter with the feature of an unsaturated reflectance, to provide wavelength selective modification of the lasing mode loss. The design criteria have been explored, with the need for low κL being highlighted, and an example with κL ~ 2 demonstrated. The engineering of the DBR number is described in order to obtain wavelength selective in-plane loss. We have shown that the addition of a DBR boundary enables lasing to occur (reducing in-plane loss) in a structure where in-plane loss would have been prohibitively high without their inclusion. The experimental band-structure was analysed, highlighting that surface emission may be enhanced at particular modes, depending upon the alignment of PhC band-structure and DBR reflectance. Control of this alignment provides a wavelength selective variation of in-plane optical loss. Such structures have the potential to realize small scale PCSELs for high-speed direct modulation. These findings offer new avenues in surface emitting laser diode engineering.

Methods

Modelling

PhC band structure simulation was carried out using 2D plane-wave expansion (PWE) with the effective refractive index method[47]. The etch depth of the PhC was measured as 240 nm for the 1.5 μm device and 200 nm for the 1.3 μm device, and was incorporated into the calculation. The effective refractive indices of the background and filled material of the PhC discussed in this paper ($n_{eff\_background}$ & n_{eff_fill}) were 3.240 and 3.195, respectively, for the 1.5 μm devices, and 3.248 and 3.215, respectively, for the 1.3 μm devices. The value of r/a for the circular PhC atoms was chosen based on the average size of hole after PhC etching. In both devices, an all-semiconductor structure was realised after regrowth[26,48].

REPCSEL resonator reflectance simulation was carried out using a transmission matrix approach via the cavity modelling framework (CAMFR) software[49], which is a fully vectorial Maxwell solver to calculate the reflectivity of the multi-layer stack. The mark/space ratio (MSR) of the DBR was defined as ~50%, corresponding to the average size of DBR after pattern transfer through the e-beam lithography and dry etch process. Since the DBR in this report is in-plane with the PhC layer and shares the same etch depth and fill factor as the PhC, the refractive index of the DBR was determined using the corresponding effective refractive indices obtained from the PhC band structure simulation. The PhC region in the simulation, as shown in the insert of Fig. 2c, was defined as a blank material with an average refractive index (n_{av}) that can be calculated using the following equation:

$$n_{av} = ff * n_{eff\_fill} + (1 - ff) * n_{eff\_background} \quad (3)$$

Where *ff* is the fill factor of the PhC.

The gap between the inner edge of DBR and the outer part of the PhC region was designed to achieve a 0° phase shift. The cavity length between two DBR groups was defined as the distance between their inner sides.

The internal resonance enhancement factor which is in term of resonator reflectance (R) can be estimated as[45]

$$\mathrm{IREF} = \frac{1}{(1 - \sqrt{R})^2} \quad (4)$$

Fabrication

Figure 6a shows a schematic of the PhC and DBR regions. For the 1310 nm REPCSEL, the PhC region was constituted of 500×500 PhC atoms and mirrors of 100 DBR periods on each side of the PhC region for a maximum reflectance calculated to be around 95%. The PhC structure had a 400 nm period constant to emit light vertically at 1.3 μm. The DBR region was defined by the 1st order Bragg condition with a 200 nm period constant. The gap between DBR and PhC regions was designed so as to have zero phase shift for reflected light. The insert shows a corresponding SEM image of the reported devices, taken after the e-beam pattern transfer. A cross-sectional view of the regrown device can also be found in Fig. 6a, highlighting the use of all-semiconductor structure and the choice of Bragg condition. Figure 6b shows a 3D schematic of the substrate emission REPCSEL device. From bottom to top, a 170 μm square aperture was employed at the n-contact for substrate emission. Following the deposition of the n-InP cladding layer, five AlGaInAs quantum wells were deposited in the intrinsic region for 1.3 μm emission. Above the epitaxial layers, an InGaAsP PhC layer was deposited. The PhC layer was positioned 125 nm above the active region. This was then patterned with the PhC and DBR structure, with a square lattice and a circular atom shape of ~0.4r/a. The DBR structure was designed to have a 50% mark-space ratio (MSR), forming the REPCSEL structure. The DBR and PhC were both dry etched to a depth of 203 nm with a CH_4/H_2- based inductively coupled plasma etch. An all-semiconductor PhC layer was created by MOVPE regrowth[26], followed by a 1.8 μm InP p-cladding layer, a 75 nm InGaAs ohmic contact layer, and a 25 nm InGaAsP current spreading layer on the top. After regrowth, a 190 μm * 190 μm square shape p-contact was deposited, above the 200 μm x 200 μm PhC region. The wafer was thinned to a thickness of ~170 μm. The 1.3 μm PCSEL device was nominally identical other than the absence of the DBR structure.

For the 1.5 μm PCSEL described in Supplementary Figs. S1, S5, S6, a similar epitaxial structure and fabrication process was used. A thicker PhC layer, with a 243 nm REPCSEL structure etch was the key difference, in addition to the active region changes. The wafer was fabricated without thinning the substrate (a 600 μm wafer thickness). Both PhC region (with 300 periods) and the DBR region (with 100 periods) were located underneath the p-contact, which gives a PhC region ~144 μm in size with a ~24 μm DBR region at each side.

Band structure measurement

As shown in Supplementary Fig. S7, the devices were electrically pumped by a pulse current source (ILX Lightwave LDP-3840) with a 2% duty cycle and a 5μs pulse width. The devices were cooled to 15 °C for room temperature measurements. An anti-reflection (AR) coated aspheric lens L1 (Thorlab AL2520M-C) with a numerical aperture (NA) of 0.54 is used to collimate the substrate-emitted light. Above it, an AR coated pellicle beam splitter PBS1 (Thorlab CM1-BP145B3) is used to reflect ~50% of the collimated surface emission in an orthogonal direction for band structure measurements. An AR coated multi-mode fiber (Thorlab M31L01) with a core diameter of 62.5μm is used to scan the reflected light in the direction of C-X and C-M, where C-M represents the oblique direction of the plane X-C-Y. An optical spectrum analyzer (OSA) (HP 70004A) measured the spectra at specific positions away from the center of the device's aperture with a 100 μm step size. The computer further integrated the measured results and generated the measured band structure. In addition to the above-mentioned optical components, two plano-convex lenses (Thorlab LA1509), L2 and L3, are used to assist with the LED light source, and a CMOS camera (Thorlab DCC-1645C) is used to image the sample surface and set up alignment.

Data availability

All the relevant data are available from the corresponding author upon reasonable request.

Received: 17 January 2024; Accepted: 28 March 2024;
Published online: 03 June 2024

References

1. Yoshida, M. et al. High-brightness scalable continuous-wave single-mode photonic-crystal laser. *Nature* **618**, 727–732 (2023).
2. Contractor, R. et al. Scalable single-mode surface-emitting laser via open-Dirac singularities. *Nature* **608**, 692–698 (2022).
3. Yang, L., Li, G., Gao, X. & Lu, L. Topological-cavity surface-emitting laser. *Nat. Photon.* **16**, 279–283 (2022).
4. Imada, M., Chutinan, A., Noda, S. & Mochizuki, M. Multidirectionally distributed feedback photonic crystal lasers. *Phys. Rev. B* **65**, 195306 (2002).
5. Kurosaka, Y. et al. On-chip beam-steering photonic-crystal lasers. *Nat. Photon.* **4**, 447–450 (2010).
6. Sakata, R. et al. Dually modulated photonic crystals enabling high-power high-beam-quality two-dimensional beam scanning lasers. *Nat. Commun.* **11**, 3487 (2020).
7. Chen, L. R., Hong, K. B., Chen, H. L., Huang, K. C. & Lu, T. C. Vertically integrated diffractive gratings on photonic crystal surface emitting lasers. *Sci. Rep.* **11**, 2427 (2021).
8. Eiji, M. et al. Lasers producing tailored beams. *Nature* **441**, 946 (2006).
9. Noda, S., Yokoyama, M., Imada, M., Chutinan, A. & Mochizuki, M. Polarization mode control of two-dimensional photonic crystal laser by unit cell structure design. *Science* **293**, 1123–1125 (2001).
10. Inoue, T. et al. Self-evolving photonic crystals for ultrafast photonics. *Nat. Commun.* **14**, 50 (2023).
11. Inoue, T., Yoshida, M., Zoysa, M. D., Ishizaki, K. & Noda, S. Design of photonic-crystal surface-emitting lasers with enhanced in-plane optical feedback for high-speed operation. *Opt. Express* **28**, 5050–5057 (2020).
12. Inoue, T. et al. General recipe to realize photonic-crystal surface-emitting lasers with 100-W-to-1-kW single-mode operation. *Nat. Commun.* **13**, 3262 (2022).
13. Morita, R., Inoue, T., De Zoysa, M., Ishizaki, K. & Noda, S. Photonic-crystal lasers with two-dimensionally arranged gain and loss sections for high-peak-power short-pulse operation. *Nat. Photon.* **15**, 311–318 (2021).
14. Yoshida, M. et al. Double-lattice photonic-crystal resonators enabling high-brightness semiconductor lasers with symmetric narrow-divergence beams. *Nat. Mater.* **18**, 121–128 (2019).
15. Itoh, Y. et al. High-power CW oscillation of 1.3-μm wavelength InP-based photonic-crystal surface-emitting lasers. *Opt. Express* **30**, 29539–29545 (2022).
16. Matsubara, H. et al. GaN photonic-crystal surface-emitting laser at blue-violet wavelengths. *Science* **319**, 445–447 (2008).
17. Ohnishi, D., Okano, T., Imada, M. & Noda, S. Room temperature continuous wave operation of a surface-emitting two-dimensional photonic crystal diode laser. *Opt. Express* **12**, 1562–1568 (2004).
18. Bian, Z. et al. 1.5 μm epitaxially regrown photonic crystal surface emitting laser diode. *IEEE Photonics Technol. Lett.* **32**, 1531–1534 (2020).
19. Hitaka, M., Hirose, K., Sugiyama, T. & Ito, A. 1.5 μm wavelength NPN-type photonic-crystal surface-emitting laser exceeding 100 mW. *Opt. Express* **31**, 18645–18653 (2023).
20. Pan, C. H., Lin, C. H., Chang, T. Y., Lu, T. C. & Lee, C. P. GaSb-based mid infrared photonic crystal surface emitting lasers. *Opt. Express* **23**, 11741–11747 (2015).
21. Chassagneux, Y. et al. Electrically pumped photonic-crystal terahertz lasers controlled by boundary conditions. *Nature* **457**, 174–178 (2009).
22. Hong, Y. H. et al. Progress of photonic-crystal surface-emitting lasers: a paradigm shift in LiDAR application. *Crystals* **12**, 800 (2022).
23. Peng, C. Y. et al. Performance analyses of photonic-crystal surface-emitting laser: toward high-speed optical communication. *Nanoscale Res. Lett.* **17**, 90 (2022).
24. Ishimura, S. et al. Proposal and demonstration of free-space optical communication using photonic crystal surface-emitting lasers. *J. Light. Technol.* **41**, 3688–3694 (2023).
25. Imada, M. et al. Coherent two-dimensional lasing action in surface-emitting laser with triangular-lattice photonic crystal structure. *Appl. Phys. Lett.* **75**, 316–318 (1999).
26. Williams, D. M. et al. Epitaxially regrown GaAs-based photonic crystal surface-emitting laser. *IEEE Photonics Technol. Lett.* **24**, 966–968 (2012).
27. Ishizaki, K., de Zoysa, M. & Noda, S. Progress in photonic-crystal surface-emitting lasers. *Photonics* **6**, 96 (2019).
28. Hirose, K. et al. Watt-class high-power, high-beam-quality photonic-crystal lasers. *Nat. Photonics* **8**, 406–411 (2014).
29. McKenzie, A. F., Kyaw, A. M., Gerrard, N. D., MacLaren, D. A. & Hogg, R. A. Kinetic influences on void formation in epitaxially regrown GaAs-Based PCSELs. *J. Cryst. Growth* **602**, 126969 (2023).
30. Li, G., Sarma, J., Taylor, R. J. E., Childs, D. T. D. & Hogg, R. A. Modeling and device simulation of photonic crystal surface emitting lasers based on Modal Index Analysis. *IEEE J. Sel. Top. Quantum Electron.* **25**, 4900309 (2019).
31. Leung, K. M. & Liu, Y. F. Photon band structures: The plane-wave method. *Phys. Rev. B* **41**, 10188–10190 (1990).
32. Kurosaka, Y., Sakai, K., Miyai, E. & Noda, S. Controlling vertical optical confinement in two-dimensional surface-emitting photonic-crystal lasers by shape of air holes. *Opt. Express* **16**, 18485–18494 (2008).
33. Kurosaka, Y. et al. Band structure observation of 2D photonic crystal with various V-shaped air-hole arrangements. *IEICE Electron. Express* **6**, 966–971 (2009).
34. Kogelnik, H. & Shank, C. V. Coupled-wave theory of distributed feedback lasers. *J. Appl. Phys.* **43**, 2327–2335 (1972).
35. Grepstad, J. O. et al. Finite-size limitations on Quality Factor of guided resonance modes in 2D Photonic Crystals. *Opt. Express* **21**, 23640–23654 (2013).
36. Ge, X., Minkov, M., Fan, S., Li, X. & Zhou, W. Low index contrast heterostructure photonic crystal cavities with high quality factors and vertical radiation coupling. *Appl. Phys. Lett.* **112**, 141105 (2018).
37. Baumann, K. et al. Organic mixed-order photonic crystal lasers with ultrasmall footprint. *Appl. Phys. Lett.* **91**, 171108 (2007).

38. Tang, R. et al. Two-dimensional heterostructure quasi-BIC photonic crystal surface-emitting laser with low divergence. *Nanophotonics* **12**, 3257–3265 (2023).
39. Kintaka, K., Majima, T., Hatanaka, K., Inoue, J. & Ura, S. Polarization-independent guided-mode resonance filter with cross-integrated waveguide resonators. *Opt. Lett.* **37**, 3264–3266 (2012).
40. Diao, Z. et al. Continuous-wave vertically emitting photonic crystal terahertz laser. *Laser Photonics Rev* **7**, L45–L50 (2013).
41. Gelleta, J., Liang, Y., Kitagawa, H. & Noda, S. Influence of external reflection on the TE mode of photonic crystal surface-emitting lasers. *J. Opt. Soc. Am. B* **32**, 1435–1441 (2015).
42. Taylor, R. J. E. et al. Mode control in photonic crystal surface emitting lasers through external reflection. *IEEE J. Sel. Top. Quantum Electron.* **23**, 4900208 (2017).
43. Iwahashi, S. et al. Higher-order vector beams produced by photonic-crystal lasers. *Opt. Express* **19**, 11963–11968 (2011).
44. Noda, S., Kitamura, K., Okino, T., Yasuda, D. & Tanaka, Y. Photonic-crystal surface-emitting lasers: Review and introduction of modulated-photonic crystals. *IEEE J. Sel. Top. Quantum Electron.* **23**, 4900107 (2017).
45. Ismail, N., Kores, C. C., Geskus, D. & Pollnau, M. Fabry-Pérot resonator: spectral line shapes, generic and related Airy distributions, linewidths, finesses, and performance at low or frequency-dependent reflectivity. *Opt. Express* **24**, 16366–16389 (2016).
46. Noda, S. et al. High-power and high-beam-quality photonic-crystal surface-emitting lasers: a tutorial. *Adv. Opt. Photonics* **15**, 977–1032 (2023).
47. Bian, Z. et al. Comparative analysis of void-containing and all-semiconductor 1.5 μm InP-based photonic crystal surface-emitting laser diodes. *AIP Adv.* **11**, 065315 (2021).
48. Wang, Z. et al. Continuous-wave operation of 1550 nm low-threshold triple-lattice photonic-crystal surface-emitting lasers. *Light Sci. Appl.* **13**, 44 (2024).
49. Bienstman P., Vanholme L., Ibanescu M., Dumon P. & Baets R. CAMFR-cavity modeling framework. [Online]. Available: https://camfr.sourceforge.net/.

Acknowledgements

This work was supported by Innovate UK Projects; “LOCAL” (Grant no. 80398), “ZEUS” (Grant no. 10049787) and “TITAN” (Grant no. 10001778). Z.Bian gratefully acknowledges financial support from the Bill Nicol Engineering Scholarship through the internal scholarship offered by the James Watt School of Engineering, University of Glasgow. Adam F. McKenzie gratefully acknowledges support from the Royal Commission for the Exhibition of 1851 through an Industrial Fellowship (Grant No. IF195/2018).

Author contributions

R.A.H., D.T.D.C., Z.B. and R.J.E.T. conceived the work. R.A.H. and R.J.E.T. supervised the research activities. Z.B., J.L., J.R.O., P.I. worked on device simulation. A.F.M. and N.D.G. developed epitaxial processes and structural characterisation of the epitaxial materials. Z.B., S.T., P.R. and J.G. developed e-beam lithography and plasma processing of the wafers. Z.B., D.K., K.J.R. and C.W.M. developed device fabrication process flow and modules. Z.B., X.Z., D.T.D.C., C.H.H. and A.S.M.K. performed device measurements. Z.B. and R.A.H. prepared the manuscript.

Competing interests

Richard A. Hogg and Richard J. E. Taylor have shares in Vector Photonics Ltd. Richard A. Hogg was seconded to Vector Photonics Ltd. by the University of Glasgow whilst engaged in this research. Zijun Bian, Connor W. Munro and Aye S.M. Kyaw were employed by Vector Photonics whilst engaged in this research. The court of the University of Glasgow has filed a patent application on aspects of the technology associated with this work (GB 2215240.9).

Additional information

Supplementary information The online version contains supplementary material available at https://doi.org/10.1038/s44310-024-00014-9.

Correspondence and requests for materials should be addressed to Zijun Bian.